Lessons from a Small Local Earthquake (M_w 3.2) That Produced the Highest Acceleration Ever Recorded in Mexico City

Shri Krishna Singh[1], Luis Quintanar-Robles[*1], Danny Arroyo[2], Victor Manuel Cruz-Atienza[1], Victor Hugo Espíndola[1], Delia I. Bello-Segura[1], and Mario Ordaz[3]

Abstract

A reliable estimation of seismic hazard-facing Mexico City from local earthquakes has suffered from poor seismic instrumentation, complex crustal structure, large and variable site amplification, and lack of knowledge of recurrence period of earthquakes on the mapped faults. Owing to recent improvement in local seismic networks, an earthquake swarm activity, which occurred in June–August 2019, was well recorded. The largest event of the sequence, an M_w 3.2 earthquake, caused panic in the city and produced peak ground acceleration (PGA) exceeding 0.3*g* at the closest station (MHVM) about 1 km away. An analysis of the event shows that it had normal-faulting focal mechanism, consistent with northeast–southwest-oriented mapped faults in the region. It was located at a depth of ~1 km and had a low stress drop (~0.1 MPa). We find that the high PGA for this low stress-drop event resulted from high-frequency amplification at MHVM (about factor of ~6 around 13 Hz), likely due to topographic site effects, superimposed on a pervasive broadband amplification of seismic waves at hill-zone sites in the Valley of Mexico (up to ~10 in the frequency band of 0.2–10 Hz). Simulation of ground motion for a scenario M_w 5.0 earthquake, using an empirical Green's function technique, reveals that such an event may give rise to significant seismic intensities in the lake-bed zone of Mexico City. The results emphasize the need to re-evaluate the seismic hazard to Mexico City from local crustal earthquakes in the Valley of Mexico.

Cite this article as Krishna Singh, S., L. Quintanar-Robles, D. Arroyo, V. M. Cruz-Atienza, V. H. Espíndola, D. I. Bello-Segura, and M. Ordaz (2020). Lessons from a Small Local Earthquake (M_w 3.2) That Produced the Highest Acceleration Ever Recorded in Mexico City, *Seismol. Res. Lett.* **91**, 3391–3406, doi: 10.1785/0220200123.

Supplemental Material

Introduction

Trans-Mexican volcanic belt (TMVB) is an east–west-oriented, Miocene to Quaternary, calc-alkaline volcanic arc related to the subduction of oceanic Rivera and Cocos plates below Mexico. TMVB is traversed by networks of faults, both parallel as well as orthogonal to its axis (Pasquaré *et al.*, 1987; Johnson and Harrison, 1990) (Fig. 1). The stress regime of the TMVB is transtensional (Mooser, 1972; Suter *et al.*, 1992, 2001; Suter, Carrillo-Martínez, *et al.*, 1995; Suter, Quintero, *et al.*, 1995; Ego and Ansan, 2002). In the central part of the TMVB (CTMVB), between 99° and 102° W, Suter *et al.* (2001) report about 100 east–west-striking, normal faults greater than 2 km in length. About 65 of these faults cut rocks less than 1.6 Ma old, and 22 are younger than 750 Ka. Although some of these faults have been studied in recent years, detailed paleoseismological studies are available for only the Venta de Bravo fault system in the Acambay graben (Langridge *et al.*, 2000, 2013; Lacan *et al.*, 2018). Mexico basin lies in the CTMVB. It is surrounded by volcanic ranges of andesitic and dacitic composition (Fig. 1, Arce *et al.*, 2019). Normal faults trending east–west and northeast–southwest have been mapped in the region. Although Mexico basin and the Valley of Mexico may technically refer to distinct areas, here we will use the terms interchangeably. Mexico City is situated within the basin.

Seismicity in the CTMVB is low. Because of sparse seismic network and complex crustal structure of the region, the earthquake locations are not sufficiently precise to map active faults, depths of the events are not well constrained, and reliable focal mechanisms are available only for a handful of earthquakes. Scarcity of data also limits our capability to estimate ground motion from future CTMVB earthquakes. For these reasons, the seismic hazard from earthquakes in the CTMVB suffers from large uncertainty (Bayona-Viveros *et al.*, 2017). Damaging earthquakes, however, have occurred in the TMVB in which 40% of the population of Mexico lives (Suárez *et al.*, 2019).

1. Universidad Nacional Autónoma de México, Instituto de Geofísica, Ciudad Universitaria, Coyoacán, Ciudad de México, Mexico; 2. Departamento de Materiales, Universidad Autónoma Metropolitana, Colonia Reynosa Tamaulipas, Ciudad de México, Mexico; 3. Universidad Nacional Autónoma de México, Instituto de Ingeniería, Ciudad Universitaria, Coyoacán, Ciudad de México, Mexico

*Corresponding author: luisq@igeofisica.unam.mx

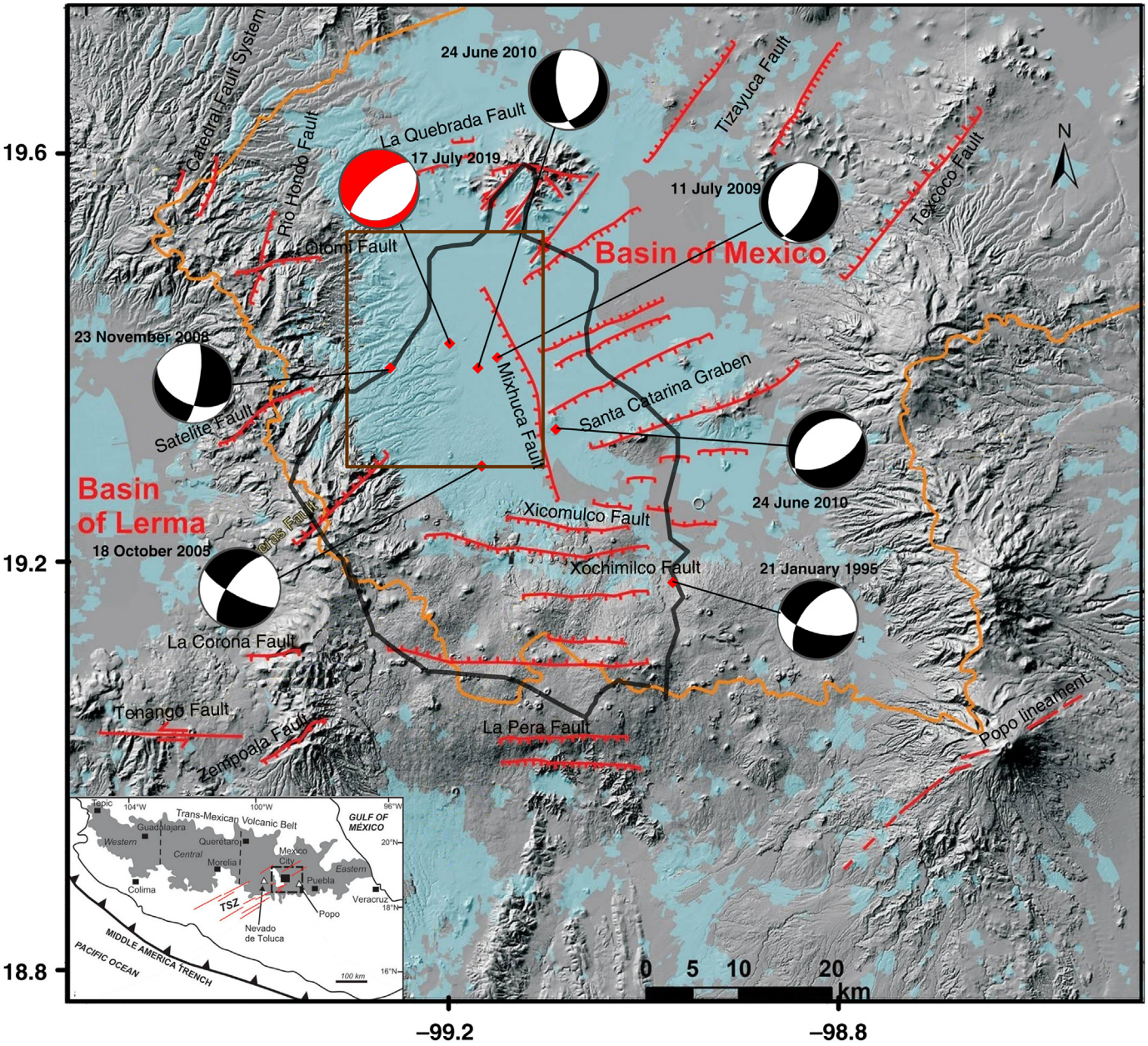

Figure 1. Geological map of Mexico basin situated within the central Trans-Mexican volcanic belt (CTMVB) showing faults and focal mechanisms of earthquakes in the region. Strike of the faulting during the 2019 event agrees with northeast–southwest orientation of mapped faults. Thick contour encloses Mexico City. The inset shows the map of Mexico in which the rectangle indicates the area covered by the figure. Modified from Arce *et al.* (2019). The color version of this figure is available only in the electronic edition.

An example is the 1912 M_s 7.0 Acambay earthquake, which caused severe damage in the epicentral area (Urbina and Camacho, 1913), although the damage in Mexico City, located about 100 km from the epicenter, seems to have been minor (Singh *et al.*, 2011). Building code of Mexico City contemplates a local **M** 4.7 earthquake (Rosenblueth *et al.*, 1989), but the analysis was based on very limited data.

There is, relatively, a long record of instrumental seismicity in Mexico City, thanks to the central seismological station at Tacubaya, which began operation in 1904. Based on Tacubaya seismograms, Figueroa (1971) estimated the annual frequency of seismic events in the valley between 1909 and 1969, and reported a tenfold increase in the last 12 yr of the interval. Alberro and Hernandez (1991) suggested a correlation between this seismicity and annual rainfall recorded at Tacubaya. Singh *et al.* (1998) reported that large earthquakes along the Mexican subduction thrust triggered seismicity in the Valley of Mexico. (A cursory examination of seismograms reveals triggered seismicity in the valley following the 8 September 2017 M_w 8.2 intraslab earthquake off the coast of Chiapas.) The seismicity in the

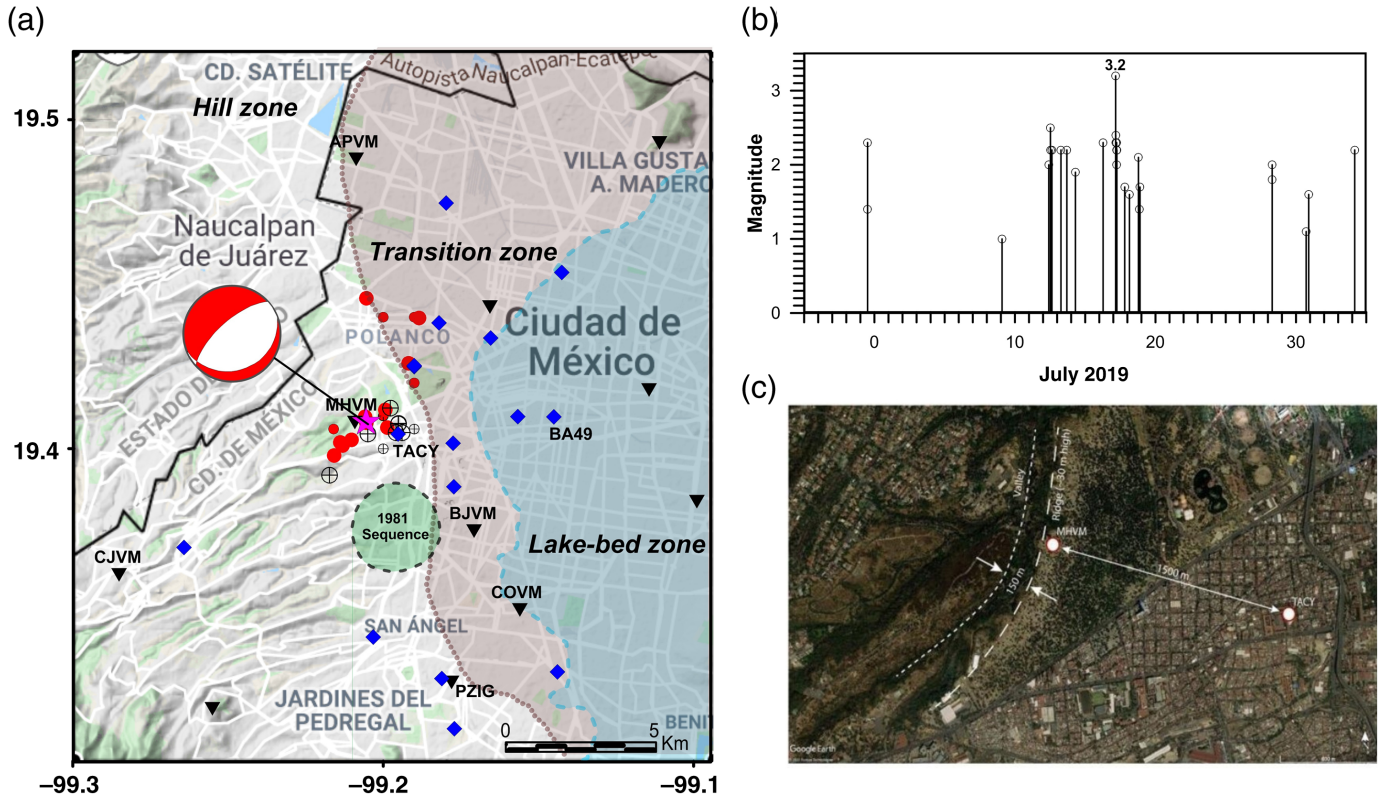

Figure 2. (a) Enlarged view of the rectangular area marked in Figure 1. Areas of hill zone, transition zone, and lake-bed zone are identified. Dashed circle is the area of 1981 earthquake swarm. Diamonds represent accelerographic station, and inverted triangles represent accelerographic + broadband station. Epicenter and focal mechanism of the mainshock (17 July 2019 M_w 3.2, 03:59) are identified. Circles enclosing cross represent foreshock, and closed circles represent aftershock; larger symbols indicate events located with double-difference technique. Stations that are mentioned in the Location of the Events and Moment Tensor (MT) Inversion of the Mainshock section are identified by their code. (b) Magnitude versus time of the seismic activity of the sequence. Much of the activity was concentrated between 12 and 19 July 2019. (c) Topographic feature of the area where the MHVM station is located. The color version of this figure is available only in the electronic edition.

valley often has swarm-like characteristics (Figueroa, 1971; Manzanilla, 1986). One such swarm, which occurred near the station Tacubaya in 1981 (Fig. 2), was studied in detail by Havskov (1982). Based on limited recordings, Lermo *et al.* (2016) reported source parameters of 14 earthquakes in the Valley of Mexico, which occurred in the period 1974–2005.

A dense network of accelerographs was installed in Mexico City following the disastrous 19 September 1985 M_w 8.0 Michoacán earthquake. Although this network produces useful recordings from moderate and large earthquakes at regional distances, it only occasionally records small, local earthquakes. In recent years, the seismic network in and around Mexico basin has been strengthened (Quintanar *et al.*, 2018). A detailed, quantitative study of some small, local earthquakes in the basin is now possible.

A swarm-like earthquake activity began on 30 June 2019 ($M_c = 2.3$) in Mexico City. The sequence was recorded by several stations in the basin, including the two nearest ones: MHVM and TACY (Fig. 2). The largest earthquake of the sequence occurred on 17 July 2019 ($M_c = 3.2$) at 03:58. Henceforth, we call it the mainshock. It produced peak ground acceleration (PGA) triplet of (101, 314, and 305 cm/s^2) on north–south, east–west, and Z components, respectively, at MHVM. The corresponding values of the PGA triplet at TACY were 40, 34, and 34.3 cm/s^2). The PGA at MHVM is the largest ever recorded at a hill-zone site in the Valley of Mexico. For comparison, the PGA triplets at CU (also a hill-zone site) during the destructive 1985 M_w 8.0 earthquakes and 19 September 2017 M_w 7.1 were 34, 33, and 21 and 34, 55, and 59 cm/s^2, respectively.

The mainshock was followed by an intense aftershock activity (Fig. 2b). The sequence was strongly felt in the epicentral area. The mainshock, with its large epicentral PGA, caused panic in the population, concern among the government authorities, and preoccupation over what might happen if a larger local earthquake were to occur in the city. The earthquake, however, caused no structural damage. We take advantage of the fact that this is the best-recorded local earthquake so far to study the source characteristics of the mainshock and the resulting ground

TABLE 1
Crustal Model

Layer	Thickness (km)	α (km/s)	β (km/s)	ρ(gm/cm^3)	Qβ*
1	2	2.90	1.58	2.50	50
2	2	4.70	2.72	2.76	50
3	26	6.60	3.81	2.82	50
4	5	7.10	4.10	3.03	50
5	∞	8.10	4.68	3.14	150

*$Q\alpha = 2Q\beta$.

motion. Preliminary simulations of ground motion from a scenario M_w 5.0 earthquake show that such an event may produce significant seismic intensities in the lake-bed zone of the city. The study highlights the need to reassess seismic hazard in the Valley of Mexico from local earthquakes.

Location of the Events and Moment Tensor (MT) Inversion of the Mainshock

Crustal model used in locating the events and in MT inversion is given in Table 1. It has been modified from Havskov (1982) and is similar to those reported by Cruz-Atienza *et al.* (2010), and Espíndola *et al.* (2017). *P*-wave velocity, α, of top two layers is based on a refraction study (Havskov and Singh, 1978). Because we analyze near-source data, the waves mostly traverse through the first two layers. For the first layer, Havskov (1982) reported $\alpha/\beta = 2.11$, in which β is the shear-wave speed. We used *P*- and *S*-arrival times from the 2019 earthquake sequence and, from Wadati diagram, estimated $\alpha/\beta = 1.84$ (Fig. S1, available in the supplemental material to this article). Thus, β in the first layer is 1.58 km/s. It follows that, at near-source distances (direct *P* and *S* waves traveling only in the first layer), R(km) = 3.47× (*S*-*P*) time. For other layers, α/β was fixed at 1.73. Density (ρ) and *S*- and *P*-wave quality factors (Q_β and Q_α) listed in the Table 1 have been chosen arbitrarily. MT inversion is not sensitive to a reasonable choice of these parameters.

In locating the mainshock, we only used phase data from stations at epicentral distance (Δ) ≤10 km [three *P* phases, one *S* phase, and six (*S*-*P*) readings]. Including farther stations increases residuals at closer stations, no doubt due to complex and heterogeneous shallow-crustal structure. The depth, H, was varied in locating the earthquake using SEISAN program (Havskov and Ottemöller, 1999). Our preferred location is 19.4090° N, 99.2090° W, $H = 0.8$ km with origin time 03:59:50.7. This location gives a minimum residual (0.33 s). We note that the hypocentral distances given by the location program differ from those obtained from (*S*-*P*) times. For example, the distances to the three closest stations, MHVM, TACY, and MT50, from the location program are 0.81, 1.73, and 2.78 km, respectively, whereas the corresponding distances from (*S*-*P*) times are 1.83, 2.78, and 4.30 km. We discuss the implication of this discrepancy later on. Although the foreshock and aftershock activities were intense, only 27 of these events were large enough to be located; the hypocenters of 18 of these could be determined using the double-difference technique (Waldhauser and Ellsworth, 2000). The locations are shown in Figure 2.

MT inversion of the mainshock was performed using algorithm ISOLA (Sokos and Zahradnik, 2008). The algorithm uses complete waveforms and Green's functions calculated using the discrete wavenumber method (Bouchon, 1981). MT solution is obtained by the least-squares, time-domain minimization of the L2-norm misfit between the observed and synthetic waveforms. We used band-passed (0.08–0.2 Hz) displacement seismograms at stations BJVM, COVM, APVM, CJVM, AOVM, and TLVM (Fig. 2). In the inversion, the epicenter was fixed at the location obtained from the phase data. The crustal model discussed previously was used in generating the Green's functions. Observed and synthetic waveforms and double-couple MT solution are shown in Figure 3. The inversion gives $H = 0.5$ km, $M_0 = 8.0 \times 10^{13}$ N · m (M_w 3.2), and NP1: $\varphi = 228°$, $\delta = 80°$, $\lambda = -97°$; NP2: $\varphi = 82°$, $\delta = 12°$, $\lambda = -57°$. As shown in Figure 3, the first motions are consistent with this focal mechanism.

For smaller events of the sequence, the signal at low frequencies is lost in the noise. At higher frequencies ($f > 1$ Hz), the Green's functions are not reliable because of complex crustal structure. The source spectrum and seismic moment of such events, as also of the mainshock, may be estimated from spectral analysis of the recordings at hill-zone sites. The time window chosen for spectral analysis brackets 95% of the energy on the horizontal components of accelerograms beginning with the arrival of *S* wave. A 5% cosine taper is applied before computing spectrum, which is then smoothed by a 1/6 octave filter. Example of data processing is shown in Figure S2.

Source Spectrum and Site Effect in the Hill Zone

It is instructive to check whether M_0 of the mainshock from MT inversion and spectral study are in agreement. The Fourier

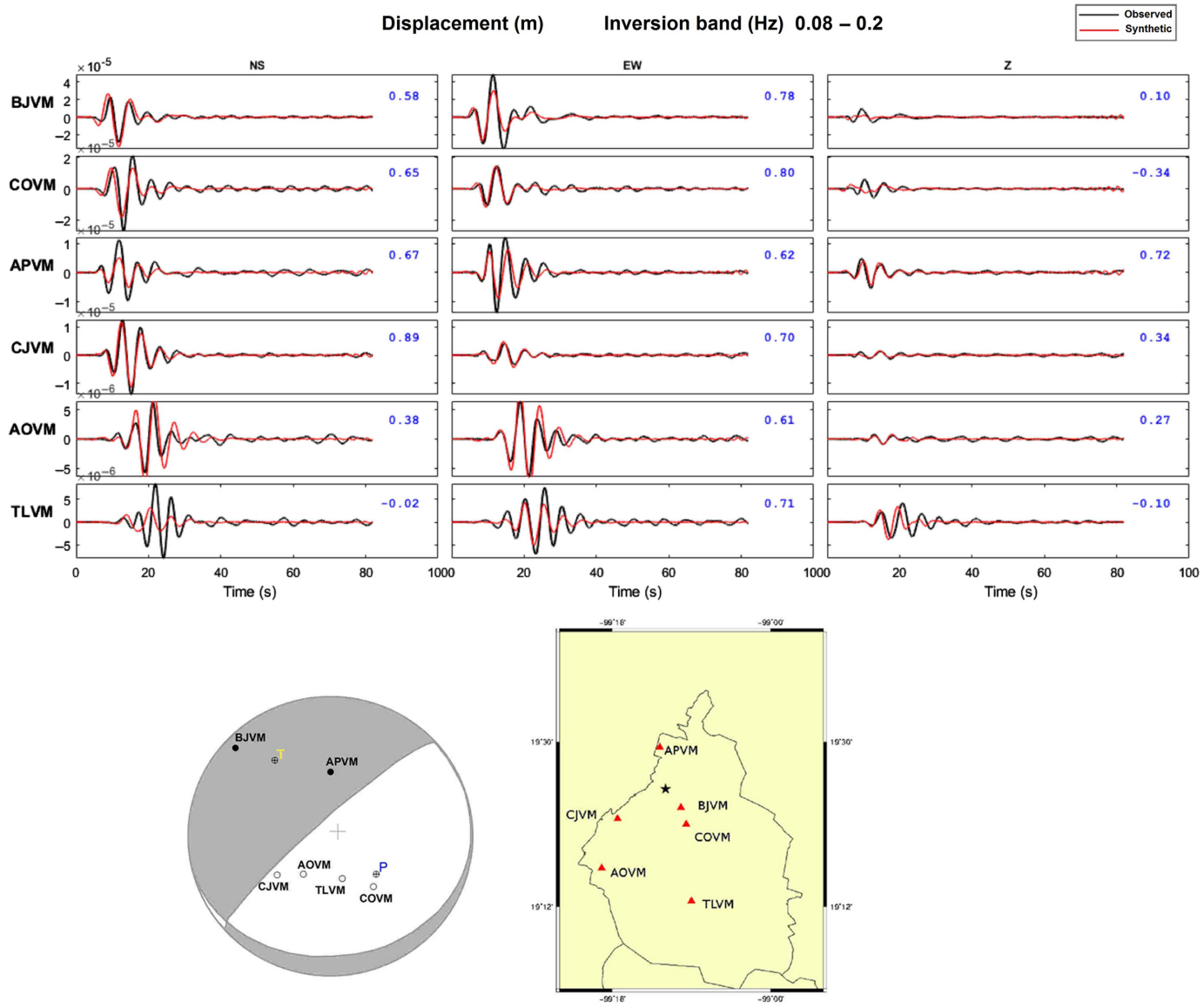

displacement spectrum, $U(f, R)$, of horizontal component of S-wave group at a site in the far field may be written as

$$U(f,R) = C \times G(R)[\{\dot{M}_0(f)\}][e^{-\pi\kappa f} B(f,fm) e^{-\pi\kappa f/\beta Q(f)} \text{Site}(f)], \quad (1a)$$

$$C = FPR\theta_\varphi/(4\pi\rho\beta^3), \quad (1b)$$

in which, $\dot{M}_0(f)$ is the source displacement spectrum (also called the moment rate spectrum), so that $\dot{M}_0(f) \to M_0$ as $f \to 0$; R is the hypocentral distance; $R_{\theta\phi}$ is the average radiation pattern (0.55); F is the free-surface amplification (2.0); P takes into account the partitioning of energy in the two horizontal components $(1/\sqrt{2})$; β is the shear-wave velocity at the source (= 1.58 km/s); and ρ is the density in the focal region (assumed here as $\rho = 2.50$ gm/cm^3). $G(R)$ in equation (1) is the geometrical spreading term. The shape of the observed spectrum, $U(f, R)$, depends on the source spectrum, $\dot{M}_0(f)$, modified by terms in the second square bracket of equation (1a). In this bracket, $Q(f)$ is the quality factor, which includes both inelastic absorption and scattering, and κ and Butterworth filter $B(f, f_m)$ account for attenuation in the near-surface layer and the finite bandwidth of the observed spectrum imposed by the sampling rate (Singh *et al.*, 1982; Boore, 1983; Anderson and Hough, 1984). Site(f) represents spectral amplification due to local site effect. Often either $B(f, f_m)$ or κ is sufficient to model the high-frequency fall off of the observed spectrum. Henceforth, we take $B(f, f_m) = 1$. As formulated previously, Site$(f) = 1$ implies the

Figure 3. Observed (band-passed 0.08–0.2 Hz) and synthetic displacement waveforms from ISOLA moment inversion (MT) inversion of the mainshock. First-motion data, shown in the focal mechanism plot, are consistent with the MT inversion. The color version of this figure is available only in the electronic edition.

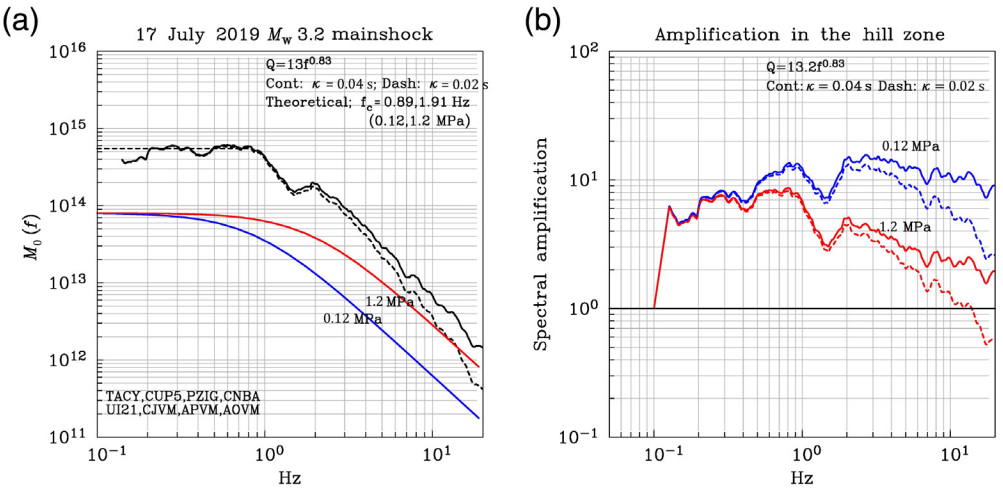

Figure 4. (a) Moment rate spectrum, $\dot{M}_0(f)$, of the mainshock from hill-zone recordings (for $\kappa =$ 0.02 and 0.04 s) and expected $\dot{M}_0(f)$ from an M_w 3.2 earthquake assuming an ω^{-2} source model and $\Delta\sigma$ of 0.12 and 1.2 MPa. (b) Ratio of $\dot{M}_0(f)$ from hill-zone recordings to the expected $\dot{M}_0(f)$ of an M_w 3.2 earthquake. The color version of this figure is available only in the electronic edition.

absence of site effect. To estimate source spectrum, $\dot{M}_0(f)$, of the earthquake, we require an estimate of $G(R)$ and $Q(f)$. Because neither $G(R)$ nor $Q(f)$ is known for the Valley of Mexico, we constrain $G(R)$ from synthetic seismograms and then estimate $Q(f)$ from observed data through equation (1).

$G(R)$

To quantify $G(R)$ for hill zone of the Valley of Mexico, we computed synthetic seismograms at an array of stations all located along the same azimuth, using discrete wavenumber method (Bouchon, 1981), and assuming infinite Q. Crustal model was discussed previously and a source at a depth of 0.8 km was taken in the calculations. Computed spectral amplitudes at some discrete frequencies as a function of R are plotted in Figure S3. The following $G(R)$ provides a reasonable approximation:

$$G(R) = (1/R), R < 3 \text{ km}, = (1/\sqrt{3R}), R \geq 3 \text{ km}.$$

$Q(f)$

Attenuation parameter, Q, in the central and eastern TMVB has been studied by several authors on a regional scale (e.g., Ortega and Quintanar, 2005; Singh *et al.*, 2007, 2017). These estimates of Q are unlikely to be valid at a small, local scale in the Valley of Mexico. We use the recordings of the mainshock to obtain a rough estimate of Q of the hill zone. Taking logarithm to the base 10 of equation (1a) gives

$$\log[U(f,R)] = \log C + \log G(R) + [\log\{\dot{M}_0(f)\} + \log \text{Site}(f) - 1.36\kappa f] - \left[1.36\left\{\frac{R}{\beta Q(f)}\right\}\right]. \quad (2)$$

The terms in the first square bracket on the right side depend on f but are independent of distance R. $Q^{-1}(f)$, and ± one standard deviation values obtained from equation (2) are plotted in Figure S4. $Q^{-1}(f)$ becomes negative between 0.4 and 1 Hz, because of amplification of seismic waves. At lower frequencies, $Q^{-1}(f)$ may not be reliable because far-filed approximation in equation (1) is violated. We, nevertheless, opt for a simple functional form for $Q^{-1}(f)$ and perform a least-squares fit to the data in the frequency range 0.1–20 Hz, which yields $Q^{-1}(f) = 0.0757f^{0.83}$ or $Q(f) = 13.2f^{0.83}$. We emphasize that $Q^{-1}(f)$ depends on $G(R)$. If we had chosen a faster decaying $G(R)$, then $Q^{-1}(f)$ would accordingly change to fit the data.

Source Spectrum

Isolated hard-site recordings of local earthquakes in the CTMVB suggest κ between 0.02 and 0.04 s (see also Lermo *et al.*, 2016; Singh *et al.*, 2017). We assume Site$(f) = 1$ in equation (2). Plots of geometric mean $\dot{M}_0(f)$ curves with $\kappa = 0.02$ and 0.04 s, computed from the horizontal-component recordings at eight stations ($2.5 < R < 20$ km), are shown in Figure 4a. The flat part of the spectrum at low frequencies ($0.2 < f < 0.8$ Hz) gives $M_0 = 5.5 \times 10^{14}$ N · m (M_w 3.76), which is 6.9 times greater than $M_0 = 8.0 \times 10^{13}$ N · m (M_w 3.20) obtained from the MT inversion. The figure also shows theoretical $\dot{M}_0(f)$ curves corresponding to M_0 from MT inversion, assuming the ω^{-2} source model of Brune (1970), and $\Delta\sigma$ of 0.12 and 1.2 MPa. (As shown later, the evidence favors $\Delta\sigma \approx 0.1$ MPa.) There is a large discrepancy between the observed and theoretical spectra. M_0 from MT inversion is reliable because of negligible site effect expected at the low frequencies (0.08–0.2 Hz) used in the MT analysis. We attribute this discrepancy to site effect in the hill zone of the Valley of Mexico. It may be argued that the disparity is due to other factors in equation (1) rather than the site effect. However, large spectral amplification in the hill zone of the Valley of Mexico has been previously reported by Ordaz and Singh (1992) and Singh *et al.* (1995), based on data from coastal earthquakes. In a later section, we compare observed ground motions with those predicted by ground-motion prediction equation (GMPE) developed by Atkinson (2015). The comparison provides independent and convincing evidence for the site effect.

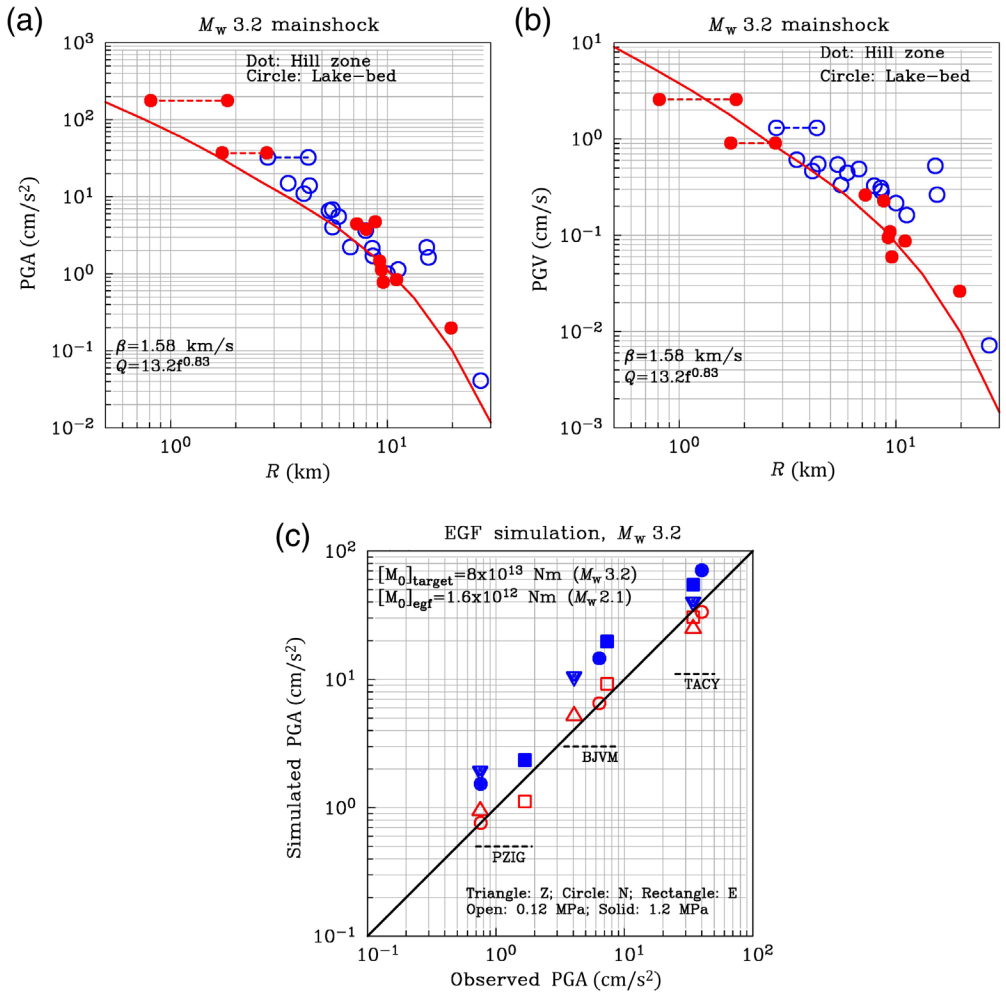

Figure 5. (a,b) Observed (dots) and predicted (via stochastic method, curves) peak ground acceleration (PGA) and peak ground velocity (PGV) for the mainshock (M_w 3.2) at hill-zone sites as a function of distance. Distances from location program as well as from (*S-P*) times are shown if $R < 5$ km. Data from lake-bed zone (circles) are plotted for comparison. (c) Observed and simulated PGA at PZIG, BJVM, and TACY for the M_w 3.2 earthquake. Simulations were performed using recordings of aftershock 5 (M_w 2.1) as empirical Green's function (EGF). Simulations with $\Delta\sigma = 0.12$ MPa for both the EGF and the target M_w 3.2 events are in good agreement with the observed data at PZIG and BJVM; choice of 1.2 MPa results in an overestimation. TACY data are better fit with $\Delta\sigma = 1.2$ MPa. The color version of this figure is available only in the electronic edition.

The ratio of observed to theoretical source spectrum provides an estimate of generic site effect in the hill zone. The estimated site effects corresponding to $\kappa = 0.02$ and 0.04 s and $\Delta\sigma$ of 0.12 and 1.2 MPa are shown in Figure 4b. We need to know $\Delta\sigma$ to choose the appropriate reference theoretical source spectrum and, thus, obtain a generic site effect in the hill zone. Unfortunately, the site effect itself makes it difficult to pick the corner frequency, f_c, and determine $\Delta\sigma$. Later, we explore spectral ratios of aftershocks to mainshock to constrain $\Delta\sigma$.

Application of Stochastic Method to Estimate Ground Motion

As mentioned previously, an estimate of $\Delta\sigma$ is needed to constrain the generic site effect in the hill zone of the Valley of Mexico. However, in our case, the estimation of ground motion from postulated events via stochastic method (Boore, 2003) does not require knowledge of true $\Delta\sigma$, provided that postulated earthquakes also follow the ω^{-2} source model, $\Delta\sigma$ is the same as for the M_w 3.2 event under study, and all the other required parameters are consistently the same. In this case, the predicted Fourier amplitude spectrum at a generic site from the postulated earthquake and, hence, also, the predicted ground-motion parameters remain the same irrespective of $\Delta\sigma$. We take advantage of this possibility and compute ground-motion parameters for M_w 3.2 and 5.0 earthquakes. Predictions for an M_w 3.2 earthquake permit comparison with the observed data, whereas those from M_w 5.0 event provide estimate of ground motions from a reasonable scenario earthquake at sites in the hill and lake-bed zones of the valley.

A parameter needed in the application of stochastic method is the effective duration, T_d, of the ground motion. T_d as a function of epicentral distance, Δ, from very shallow earthquakes in the Valley of Mexico has not been studied previously due to lack of data. The recordings of the mainshock in the hill zone permit us to find a preliminary relation between T_d and Δ. We define T_d as the duration that brackets 5%–95% of the energy in the accelerogram. The data for hill-and lake-bed zones are plotted in Figure S5. As expected, T_d increases with Δ and, also, as expected, it is greater in the lake-bed zone. The fit to the hill-zone data is given by $(T_d - 1/f_c) = 0.93\Delta$, in which f_c is the corner frequency, taken here as 1 Hz for the mainshock.

Calculations using the stochastic method were made assuming Brune ω^{-2} source model with $\Delta\sigma = 0.12$ MPa, $\beta = 1.58$ km/s, $\rho = 2.50$ gm/cm^3, $\kappa = 0.02$ s, $G(R)$ and Q(f) defined previously, and Site(f) corresponding to $\Delta\sigma = 0.12$ MPa (Fig. 4b). Figure 5a,b compares predicted PGA and peak ground velocity (PGV) for an M_w 3.2 earthquake

TABLE 2
Peak Ground Acceleration (PGA) of Some Earthquakes Recorded at MHVM and TACY

Event (yyyy/mm/dd hh:mm)	Station	North–South (cm/s^2)	East–West (cm/s^2)	Z (cm/s^2)
2019/07/12 12:38, foreshock	MHVM	17.7	33.3	21.5
	TACY	17.9	16.5	11.5
2019/07/17 03:59, mainshock	MHVM	101.0	314.0	305.0
	TACY	40.1	34.3	34.3
2019/07/17 04:10, aftershock 1	MHVM	19.1	122.0	74.0
	TACY	6.7	7.6	5.5
2019/07/17 04:18, aftershock 2	MHVM	23.7	102.0	48.1
	TACY	6.8	8.1	6.2
2019/07/17 05:33, aftershock3	MHVM	16.4	57.2	29.3
	TACY	2.6	2.6	3.3
2019/07/17 05:41, aftershock 4	MHVM	12.1	35.3	32.4
	TACY	4.4	5.4	4.4
2019/07/17 05:45, aftershock 5	MHVM	18.6	116.0	56.5
	TACY	4.5	4.3	3.8
2018/02/16 M_w 7.2	MHVM	7.9	9.3	3.8
	TACY	7.6	8.7	3.9
2018/07/19 M_w 5.9	MHVM	2.1	2.1	1.7
	TACY	1.5	1.5	1.5
2017/09/19 M_w 7.1	MHVM	22.7	80.0	50.9
	TACY	58.4	62.4	34.6
2017/09/08 M_w 8.2	MHVM	7.1	7.57	4.3
	TACY	8.1	8.0	4.6

at hill-zone sites with the observed values during the mainshock of the sequence. Observed data from the lake-bed zone are also plotted in the figure for comparison. We note that predicted values of PGA and PGV at hill-zone sites agree well with the observed ones, except at the two nearest sites, MHVM and TACY. If R to these two sites is taken from the location program, then the PGA values are well predicted, but PGV values are slightly low. If R is taken from (S-P) time, then the observed PGA is very high, but PGV is well predicted. We consider R computed from (S-P) time to be more accurate and investigate the cause of high PGA at MHVM and TACY in a later section.

Stress Drop

As mentioned previously, it is difficult to estimate $\Delta\sigma$ of the mainshock from the source spectrum, because the site effect masks the corner frequency f_c. Yet, $\Delta\sigma$ is critical to gauge the strength of the relatively shallow faults ($H \sim 1$ km) in the Valley of Mexico and to isolate the site effect. It is also a crucial parameter in the estimation of ground motion from postulated earthquakes.

A powerful alternative is to estimate f_c from spectral ratios of well-recorded aftershocks to mainshock. We selected five of the larger aftershocks for analysis. These events occurred on the same day as the mainshock (Table 2) and were well recorded at MHVM, TACY, PZIG, and BJVM. The analysis assumes that all events are collocated and have the same focal mechanism. Stations MHVM and TACY were not used in the analysis, as they were too close to the sources. The spectral ratios (geometric mean of north–south, east–west, and Z ratios) at stations PZIG and BJVM are shown in Figure 6. For reference, in each frame, we show the spectral ratios corresponding to Brune ω^{-2} source model with constant $\Delta\sigma$ (i.e., the same $\Delta\sigma$ for the aftershocks and the mainshock of 0.12 and 1.2 MPa). The observed ratios clearly favor f_c of about 0.9 Hz (0.12 MPa) and support ω^{-2} source with constant $\Delta\sigma$. In any case, $\Delta\sigma \geq 1$ MPa($f_c \geq 1.9$ Hz) seems very unlikely. For some aftershock-mainshock pairs, a better fit (albeit marginally so) is

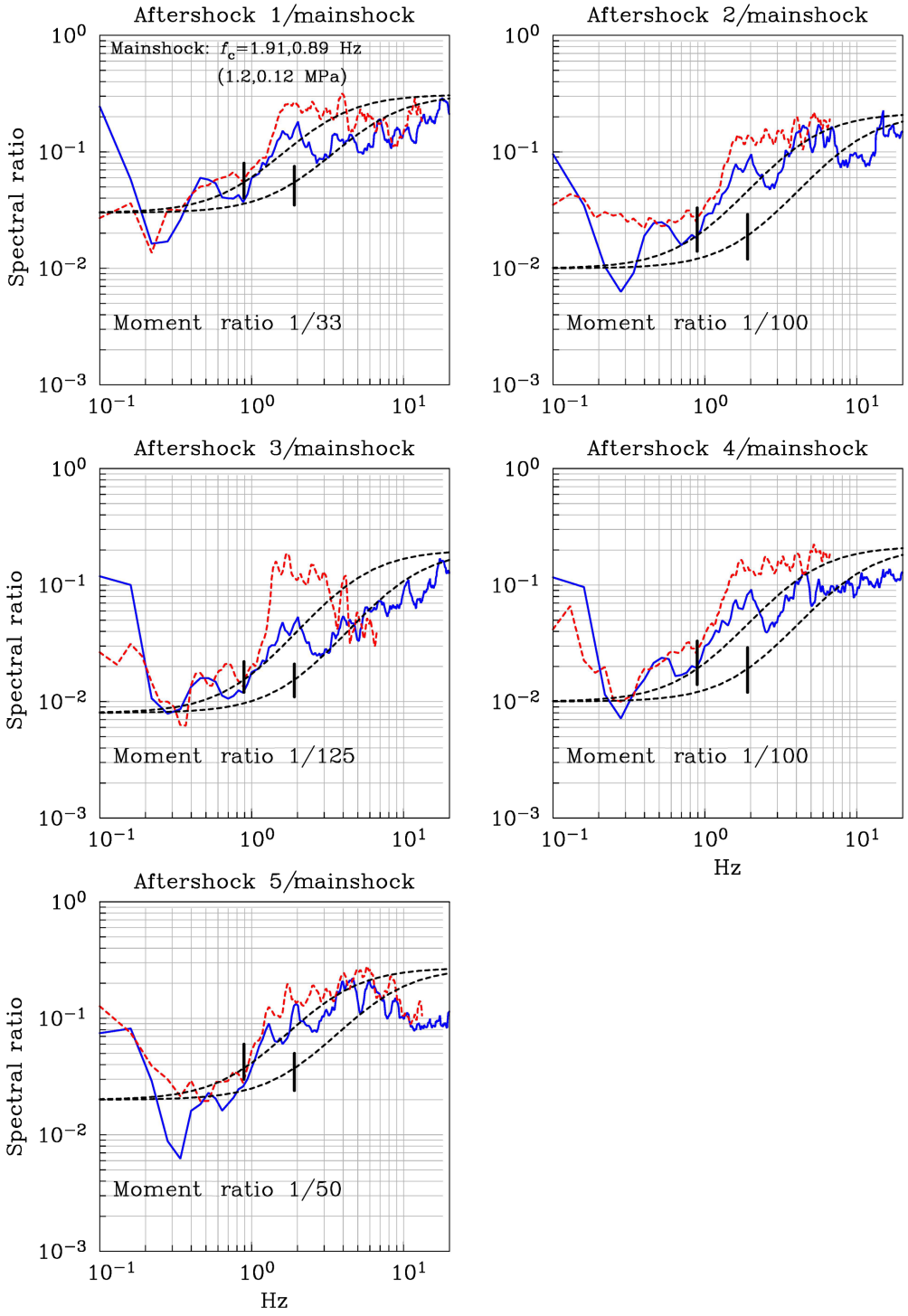

Figure 6. Spectral ratios of five of the larger aftershocks (Table 2) to the mainshock at BJVM and PZIG. Ratio at each station is the geometric mean of north–south, east–west, and *Z* ratios. Dashed lines represent BJVM, continuous lines represent PZIG, and smooth dashed lines represent theoretical curves for an ω^{-2}, constant $\Delta\sigma$ source model. Curves corresponding to $f_c = 0.89$ and 1.91 Hz ($\Delta\sigma = 0.12$ and 1.2 MPa) for the mainshock are illustrated in the figure. Short vertical lines mark f_c of 0.89 and 1.91 Hz. Observed ratios suggest $f_c = 0.89$ Hz ($\Delta\sigma = 0.12$ MPa) for the mainshock. The color version of this figure is available only in the electronic edition.

obtained with an ω^{-2} source with increasing $\Delta\sigma$ ($\Delta\sigma\alpha M_0^{1/4}$) (not shown in the figure). An ω^{-3} source is unacceptable (not shown in the figure).

To further test whether $\Delta\sigma$ was low during the earthquake sequence, we synthesized PGA of an M_w 3.2 target event using the recordings of the aftershock 5 (M_w 2.1) at stations BJVM, PZIG, and TACY as empirical Green's functions (EGFs). A method developed by Ordaz *et al.* (1995) and modified by Khors-Sansorny *et al.* (2005) was used in the synthesis. It assumes that far-field approximation is valid. The summation scheme obeys the ω^{-2}-source scaling at all frequencies and produces realistic time histories. The method requires specification of only the seismic moments and stress parameters of EGF and target events. We assumed same $\Delta\sigma$ for both events. Calculations were performed for $\Delta\sigma$ of 0.12 and 1.2 MPa. As seen in Figure 5c, the simulations with $\Delta\sigma = 0.12$ MPa are in good agreement with the observed PGA at PZIG and BJVM, whereas calculations with $\Delta\sigma = 1.2$ MPa result in an overestimation. TACY data are better fit with $\Delta\sigma = 1.2$ MPa. This discrepancy may be due to the assumption that the two events are collocated, which may not be valid at TACY due to the station's proximity to the sources.

Low Stress Drop but High PGA at MHVM

If the stress drop was low, why, then, was the PGA at MHVM so high at least on the EW component? In search of an

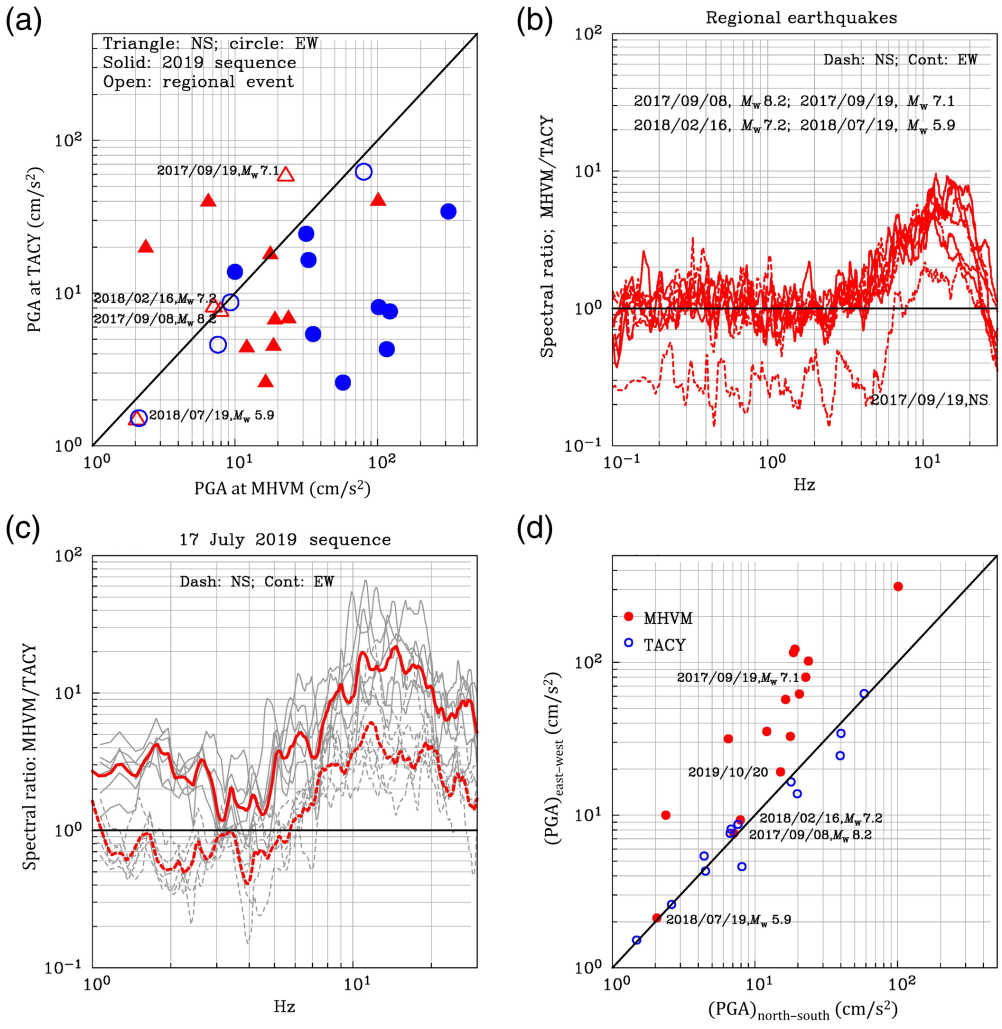

Figure 7. Comparison of ground motion at MHVM and TACY. (a) PGA at MHVM versus at TACY for events of the 2019 sequence and regional earthquakes. For most events of the 2019 sequence, the PGA at MHVM is greater than at TACY, especially on the east–west component (solid symbols). For regional earthquakes (130 < R < 750 km), PGA is about the same at the two stations (open symbols) with one exception (north–south component, 19 September 2017 M_W 7.1). (b) Spectral ratio, MHVM-TACY, for regional earthquakes. north–south and east–west ratios are nearly the same with one exception (north–south ratio, 19 September 2017 M_W 7.1). (c) Spectral ratio, MHVM-TACY, for the 17 July 2019 earthquake sequence. Ratio of individual events and geometric mean curves is shown for north–south and east–west components separately. (d) PGA on east–west component versus PGA on north–south component of recordings at MHVM and TACY. Some events, discussed in the Low Stress Drop but High PGA at MHVM section, are identified in the frames. The color version of this figure is available only in the electronic edition.

answer, we analyzed recordings at MHVM and the nearby station TACY (station separation 1.5 km) of the 2019 sequence and four regional events (5.9 ≤ M_w ≤ 8.2; 127 ≤ R ≤ 750 km). The results are summarized in Figure 7. PGAs of the same event at these two stations are compared in Figure 7a. For most events of the 2019 sequence, the PGA at MHVM is greater than at TACY (solid symbols). In addition, the amplification of PGA on east–west component at MHVM compared to TACY is generally greater than that on the north–south component (compare solid circles and triangles in the figure). For regional earthquakes, the PGA is about the same at the two stations (open symbols), with the exception of north–south component at MHVM of the 19 September 2017 M_w 7.1 earthquake. One explanation of larger PGA at MHVM as compared to TACY for the 2019 sequence could be shorter hypocentral distances of the former station than the latter. This would also explain nearly equal PGA at the two stations during regional events, because distance would not be a factor in this case.

Spectral ratio, MHVM-TACY, of the regional earthquakes are illustrated in Figure 7b. We note that the north–south and east–west ratios are similar with one exception. The ratios are about 1 for f < 3 Hz. At higher frequencies both north–south and east–west components at MHVM are amplified with respect to TACY, showing fairly broadband amplification in the range 3–25 Hz, which reaches about 6 around 13 Hz. This suggests that high-frequency site effect at MHVM was, at least, partly responsible for high-observed PGA. The exception mentioned previously is the spectral ratio of north–south component of the 2017 M_w 7.1 earthquake, which is about one fourth of the general trend of the ratios over the entire frequency range 0.1–25 Hz. Figure S6 shows Fourier acceleration spectra of the mainshock and five of the aftershocks of the 2019 sequence listed in Table 2. Figure 7c illustrates spectral ratios. Although there is a broadband amplification of both components of MHVM, the geometric mean amplification of east–west component is about five times greater than the north–south component. This differs from the regional earthquakes for which north–south and east–west spectral ratios are nearly equal with the one exception mentioned previously

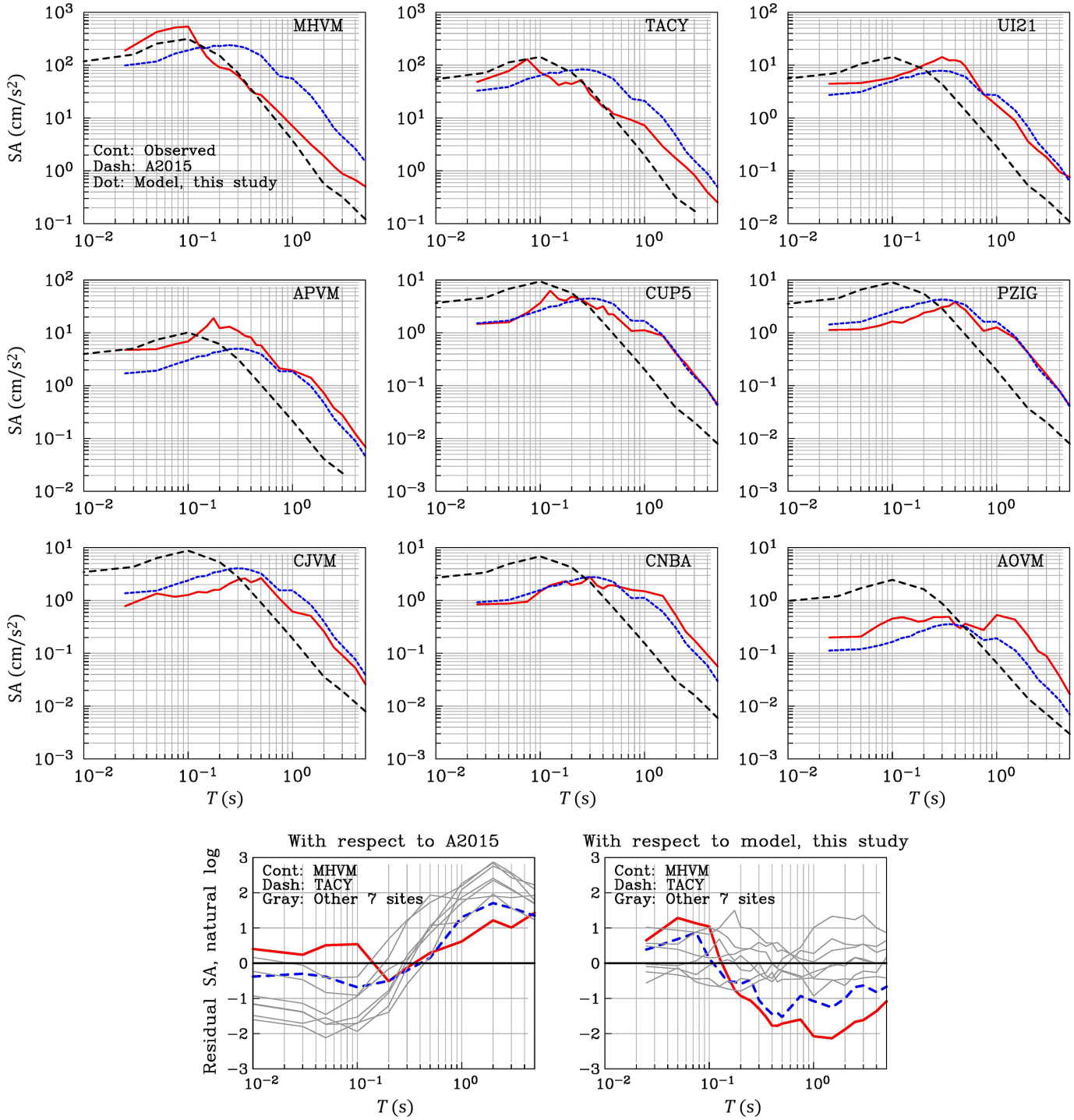

Figure 8. Comparison of observed spectral acceleration (SA) of the M_w 3.2 mainshock with predicted SA from ground-motion prediction equation (GMPE) of Atkinson (2015) and from stochastic method (this study). Bottom two panels show residual with respect to SA from GMPE of Atkinson (2015) and predicted SA using stochastic method in this study. The color version of this figure is available only in the electronic edition.

(Fig. 7b). Figure 7d shows plot of $(PGA)_{east-west}$ versus $(PGA)_{north-south}$ at MHVM and TACY. At TACY, $(PGA)_{east-west}$ is about the same as $(PGA)_{north-south}$ for all events, as expected. However, $(PGA)_{east-west}$ at MHVM is about 3.5 times $(PGA)_{north-south}$ for the local earthquake sequence of 2019 and for the 2017 M_w 7.1 intraslab earthquake.

In view of unusual characteristics of ground motion at MHVM compared to TACY, illustrated in Figure 7, we checked the performance of the accelerograph at MHVM by installing a seismograph at the same site. A local event on 20 October 2019

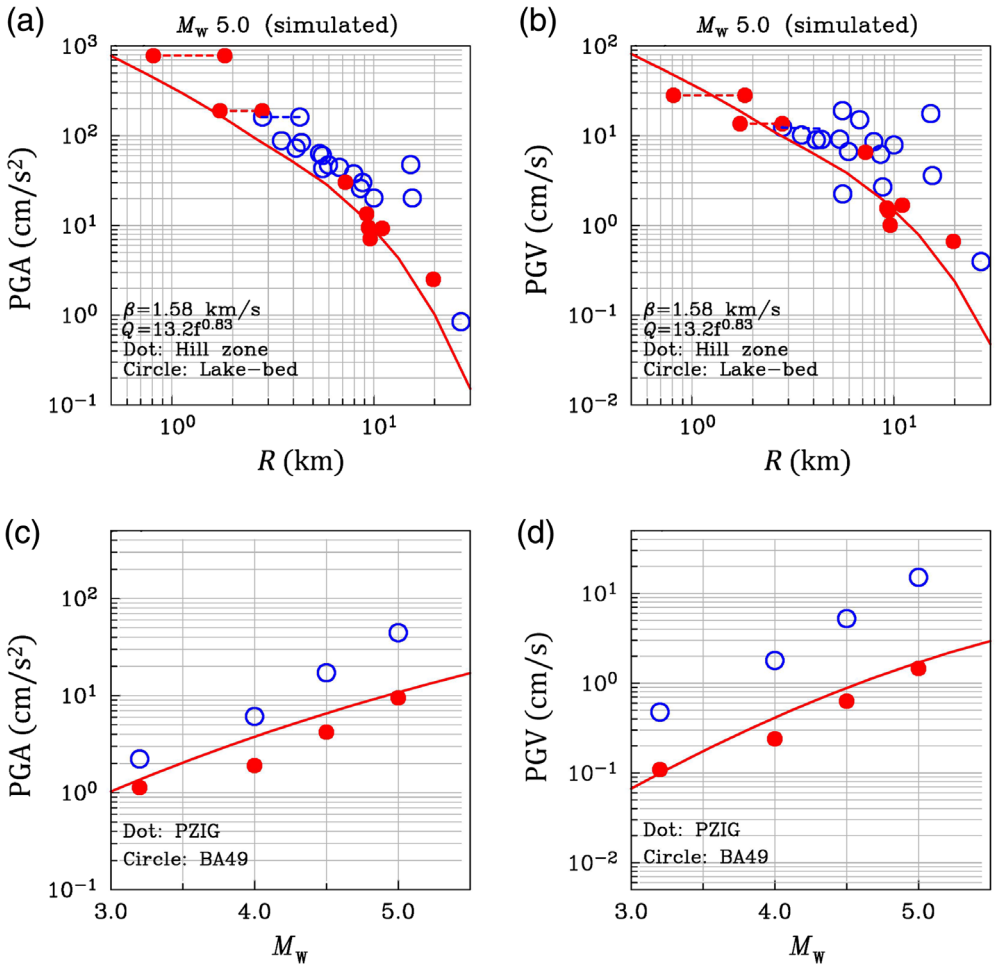

Figure 9. (a,b) Predicted PGA and PGV for a postulated M_w 5.0 earthquake. Predictions at hard sites via stochastic method are illustrated by curves. Symbols (dots represent hill zone and open circles represent lake-bed zone) show simulated values using an EGF summation technique with the recordings of M_w 3.2 mainshock as EGF. (c,d) Scaling of PGA and PGV with M_w at BA49 (soft site) and PZIG (hill-zone site) computed using EGF technique. Predictions at hard sites via stochastic method are illustrated by curves. The color version of this figure is available only in the electronic edition.

was recorded by both instruments. PGA, PGV, and spectra of the event recorded by the two systems were almost identical, confirming proper functioning of the accelerograph at MHVM during this event. Curiously, for this event, $(PGA)_{east-west}$ roughly equals $(PGA)_{north-south}$, similar to the regional earthquakes. This does not guarantee that the accelerograph was working well during all events listed in Table 2. The fact that the north–south spectral ratio at MHVM during the 19 September 2017 earthquake is about one-fourth of the east–west spectral ratio, in the 0.1–25 Hz range (Fig. 7b), argues against it. It is possible that the response of the north–south component of accelerograph is erratic. If, however, the response of the accelerograph is correct, then MHVM suffers from an unusual site effect, perhaps caused by the topographic ridge where the station is located, which is 25–30 m high with respect to a topographic depression (valley) lying next to the ridge (Fig. 2c). As mentioned earlier, spectral amplification at MHVM sharply increases from 3 to 4 Hz and reaches its maximum around 10–15 Hz, with most values exceeding 10 in the east–west component (Fig. 7c). Topographic site effect (TSE) is well known to produce significant ground-motion variability at short distances (Maufroy *et al.*, 2012, 2015, 2018; Hartzell *et al.*, 2017) and maximizes where the characteristic (horizontal) length of the topographic features is similar to half the *S* wavelength. Although TSE depends also on the topographic curvature (Maufroy *et al.*, 2015), characteristic lengths susceptible to explain amplifications at MHVM thus range between 50 and 80 m (i.e., assuming V_S of layer one in Table 1), which are scale consistent with the terrain variations found at the site (Fig. 2c). Directionality of TSE has also been reported and depends on both the relative source-site position and the orientation of the topographic feature (Hartzell *et al.*, 2017). Because the MHVM site lies on top of a ridge with local north–south orientation, larger amplification (Fig. 7c) and PGAs (Fig. 7d) observed in the east–west component for regional and local earthquakes could be explained by very local TSE. We have documented site amplification at MHVM, albeit an unusual one. Thus, high PGA at MHVM, which was most likely caused by a site effect, does not contradict a low stress drop during the earthquake.

Further Support for Site Effect

In the previous section, we have shown evidence of large high-frequency amplification at MHVM. Earlier, we attributed the disparity between observed and theoretical source spectra to pervasive broadband site effect at hill-zone sites of Mexico City. Further compelling support for these site effects comes from the comparison of observed response spectra, SA, with prediction from GMPE of Atkinson (2015), henceforth called A2015. The GMPE was developed from recordings of **M** ≤ 6 California earthquakes at distances ≤40 km. The comparison is shown in Figure 8, in which spectral acceleration

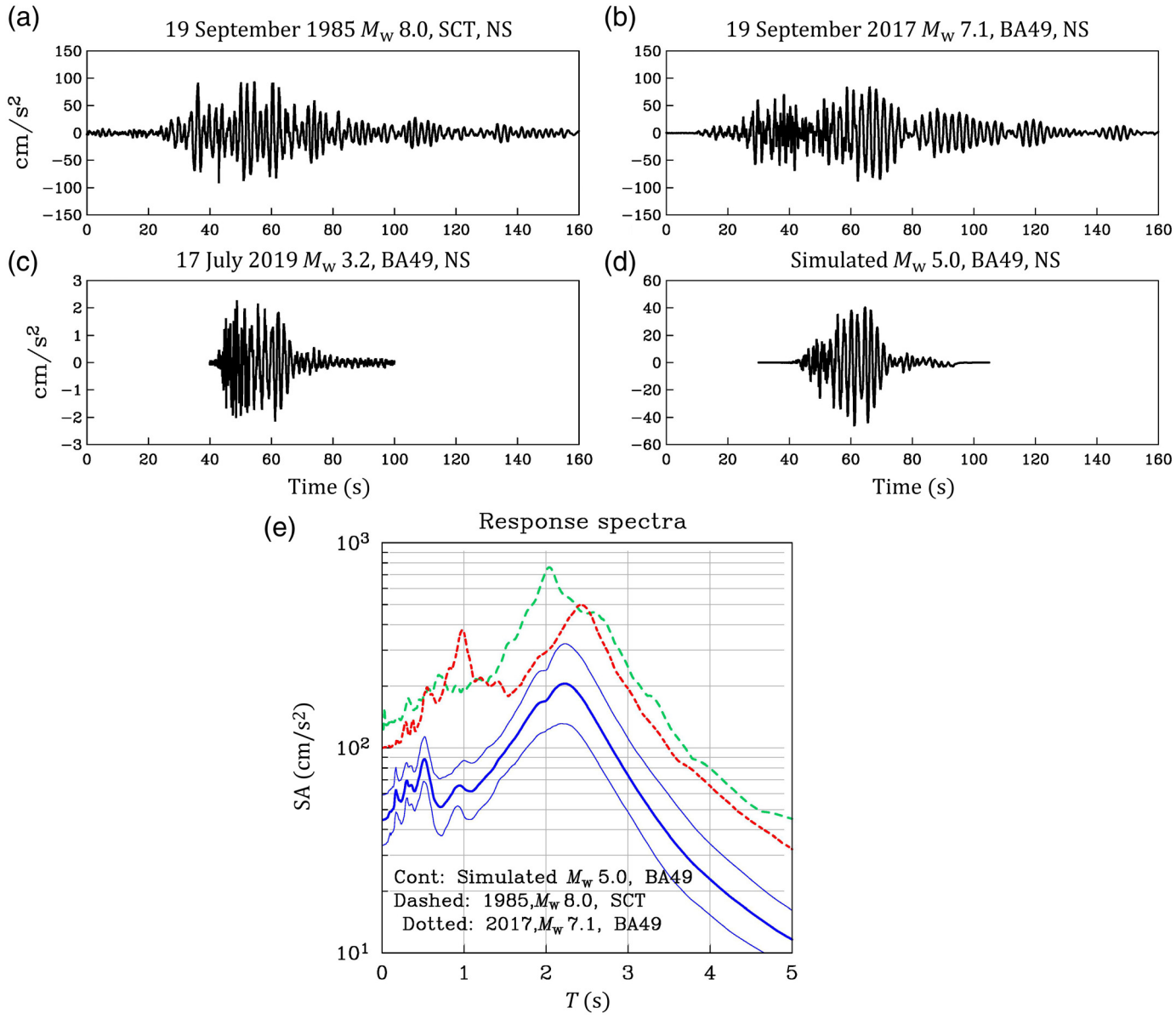

Figure 10. Comparison of observed ground motion during the devastating earthquakes of 1985 M_w 8.0 and 2017 M_w 7.1 with the expected motion from a scenario M_w 5.0 event. North–south acceleration (a) at SCT in 1985 (R = 300 km), (b) at BA49, a site nearby SCT, in 2017 (R = 127 km), (c) at BA49 during 2019 M_w 3.2 earthquake (R = 6.8 km), (d) at BA49 from postulated M_w 5.0 earthquake using EGF technique. (e) SA, 5% damping, of 1985, 2017, and postulated M_w 5.0 earthquakes. SA is the geometric mean of the two horizontal components. The color version of this figure is available only in the electronic edition.

(SA) predicted in this study via stochastic method is also included. The bottom two panels illustrate residuals with respect to A2015 and stochastic prediction from this study. We note that, at smaller periods, A2015 overestimates observed SA at most stations, while underestimating at MHVM. The opposite is true at longer periods, except at MHVM and TACY. This is consistent with high-frequency site amplification at MHVM and pervasive broadband amplification at hill-zone sites. As expected, the stochastic prediction developed in this study fits the observed SA well at all sites except the nearest two.

Ground Motion from a Scenario M_w 5.0 Earthquake

There are several mapped normal faults in the Valley of Mexico exceeding 20 km in length (Fig. 1). A 20 km long rupture corresponds to an $M_w \approx 6.5$ earthquake (Wells and Coppersmith, 1994). Here, we consider a scenario earthquake of M_w 5.0, although larger earthquakes are plausible. We estimate ground motions from such an event, applying the stochastic and EGF techniques. Both techniques assume that far-field approximation is valid, that is, distance to station, R, is much greater than both the source dimension as well the wavelength of interest.

Expected rupture length of an M_w 5.0 earthquake is about 3–4 km (Wells and Coppersmith, 1994). The period of interest in Mexico City is less than about 2.5 s, so that, for $\beta = 1.58$ km/s, the wavelength of interest is <4.0 km. It follows that, for far-field approximation to be valid, R should be much greater than 4.0 km. Although we present predicted ground motions at shorter distances, the results for $R < 6.0$ km are likely to be approximate.

The parameters used in the stochastic simulation, valid for hill-zone sites only, are the same as those used in the simulation of M_w 3.2 earthquake. In the EGF simulation, we used the M_w 3.2 mainshock as the EGF and assumed the same stress drop, 0.12 MP, for both the EGF and target events. The results are shown in Figure 9a,b. We ignore stations at $R < 5$ km, because of uncertainty in the location discussed earlier, and the failure of far-field approximation. At $R > 5$ km, stochastic and EGF predictions at hard sites are similar. We note that the simulated PGA values at soft sites for an M_w 5.0 earthquake, using the EGF technique, are higher than at hard sites by a factor greater than those observed during the M_w 3.2 mainshock (compare Figs. 5a and 9a). It is further accentuated for PGV (compare Figs. 5b and 9b). This implies that the scaling of PGA and PGV with M_w differs for hard and soft sites. It is confirmed from Figures 8d and 9c, which show the scaling at hard hill-zone site PZIG ($R = 9.4$ km) and soft lake-bed zone site BA49 ($R = 6.8$ km) (Fig. 2), the dependence of PGA and PGV on M_w is greater at the soft site. The stochastic predictions for PZIG ($R = 9.4$ km) agree reasonably well with EGF calculations, especially for M_w 5.0. Different M_w scaling is likely a consequence of harmonic nature of the ground motion at the lake-bed zone site of BA49 (natural frequency 0.5 Hz), which is not the case at PZIG located in the hill zone.

The predicted PGA and PGV from EGF technique at BA49 of 45 cm/s^2 and 15 cm/s (Fig. 9) are smaller than those recorded during the destructive earthquakes of 19 September 2017 M_w 7.1 (100 cm/s^2, 34 cm/s) at BA49 and 19 September 1985 M_w 8.0 (124 cm/s^2, 45 cm/s) at SCT located nearby BA49. (BA49 had not been installed when 1985 earthquake occurred.) Figure 10a–d illustrates north–south accelerograms of the two destructive earthquakes, the M_w 3.2 event used as the EGF, and simulated M_w 5.0 earthquake. The geometric mean of the response spectra (SA) of the events are shown in Figure 10e. The figure illustrates that the postulated M_w 5 event may produce significant seismic intensities in the lake-bed zone of Mexico City. We note that a higher but equal stress drop of the EGF and target events will produce larger simulated motions; the same is true if the EGF stress drop is taken as 0.12 MPa but a large value is chosen for the target event. An extrapolation of PGA and PGV versus M_w plots in Figure 9c,d suggests peak values similar to those observed in 1985 and 2017 for an M_w 5.5 event. Although such an extrapolation is not valid since point source, far-field approximation is grossly violated, it is clear that $M_w \geq 5.5$ events present, potentially, significant hazard to Mexico City.

Discussion and Conclusions

The 2019 earthquakes were the best-recorded local events in Mexico City thus far. From an analysis of the sequence, we find that:

1. The seismic activity began on 30 June 2019 ($M_c = 2.3$), and the largest earthquake occurred on 17 July 2019 at 03:59. An intense aftershock activity followed during the next 24 hr and continued till 20 October 2019.
2. The depth of the events in the sequence was less than about 1 km, similar to the depth reported for the 1981 sequence, which occurred about 3 km to the south. We find that at this depth the ratio of P-wave to S-wave speed, α/β, is 1.84 as compared to 1.73 for a Poisson's solid. High value of the ratio may be due to the presence of water in the rocks at 1 km depth.
3. MT inversion of band-pass filtered (0.08–0.2 Hz) displacement traces yields $M_0 = 8.0 \times 10^{13}$ N · m and a normal-faulting event with NP1: $\varphi = 228°$, $\delta = 80°$, $\lambda = -97°$; and NP2: $\varphi = 82°$, $\delta = 12°$, $\lambda = -57°$. First-motion data are in agreement with this mechanism. Northeast–southwest strike of the fault agrees with the mapped faults in the area (Figs. 1 and 2). Presumably, NP1, which dips steeply to the northwest, is the fault plane.
4. A relatively large amplification of seismic waves occurs in the hill zone of the valley, confirming previous results from the analysis of regional earthquakes. A consequence of this amplification is that the moment magnitude, M_w, of local earthquakes is likely to be overestimated, unless frequencies less than 0.2 Hz are used in the magnitude estimation. Because of the cultural noise, this is only possible for $M_w >$ 3 events in the valley.
5. Complex, unmapped, 3D crustal structure of the valley, and the site effect lead to unreliable determination of hypocenter and make it difficult to determine the corner frequency and, hence, the stress drop.
6. Although the corner frequency of the mainshock cannot be picked on the source spectrum with confidence, the spectral ratios of aftershocks to the mainshock supports a very low stress, ≈0.1 MPa. The stratigraphy in the source region comprises of Oligocene volcanics overlain by Miocene volcanics with a total thickness of about 2 km, on top of which are found about 100 m thick tuffs. These volcanics at shallow depth probably have low strength and rupture in low stress-drop events.
7. High PGA at the closest station MHVM was caused by amplification of high frequencies, likely due to local TSEs associated with a north–south-oriented ~30 m high ridge where the station is located. Such topographic feature could explain the systematically higher PGAs observed in the east–west component. There is no contradiction with a low stress-drop event producing high PGA at MHVM.
8. We estimated ground motions from an M_w 5.0 scenario earthquake. Mainshock recordings of the 2019 sequence

were used as EGFs. The results reveal that such an event may give rise to significant intensities in the lake-bed zone of Mexico City. There are numerous mapped faults in the Valley of Mexico, which exceed 20 km in length. Thus, $M_w > 5.0$ earthquakes cannot be ruled out. Reliable synthesis of ground motion from such earthquakes would require careful consideration of finite-fault and near-field effects. A vigorous research effort is urgent to re-evaluate seismic hazard posed by local, crustal earthquakes in the Valley of Mexico and elsewhere in TMVB.

9. The analysis of the 2019 sequence exemplifies some of the difficulties that such an endeavor will entail. Additional seismic and accelerographic stations, especially at very hard sites in the hill zone, and revival of bore-hole instrumentation, currently abandoned, will be helpful in source studies. We also need to improve our knowledge of the subsoil conditions, velocity models, and attenuation of seismic waves. This would result in more reliable earthquake locations and estimation of ground motions from finite-fault, physically based simulations.

Data and Resources

Data used in this study were obtained by the National Seismological Service (SSN; http://www.ssn.unam.mx/doi/networks/mx/), Instituto de Geofísica, Universidad Nacional Autónoma de México (UNAM); the Strong Ground Motion Database System (http://aplicaciones.iingen.unam.mx/AcelerogramasRSM/); and the Centro de Instrumentación y Registro Sísmico (CIRES; http://cires.org.mx/registro_es.php), Mexico City. All websites were last accessed on January 2020.

Acknowledgments

The authors acknowledge incisive comments by Reviewers Gail Atkinson and Dino Bindi. The authors also thank the personnel of National Seismological Service (SSN), Instituto de Geofísica, Universidad Nacional Autónoma de México (UNAM); Seismic Instrumentation Group at the Instituto de Ingeniería of the National Autonomous University of Mexico (UNAM); and the Centro de Instrumentación y Registro Sísmico (CIRES) for station maintenance as well as data acquisition and distribution. The authors deeply acknowledge the support received from government authorities of Mexico City through their Secretaría de Educación, Ciencia, Tecnología e Innovación for acquisition of seismological equipments and its deployment through Funding Agreement SECTEI/194/2019. The research was partly supported by Dirección General Asuntos del Personal Académico (DGAPA), UNAM Projects IN101018 and IG100617, and Consejo Nacional de Ciencia y Tecnología (CONACyT) Project 6471.

References

Alberro, J., and R. Hernández (1991). *Temblores inducidos por fuerzas de filtración*, Rept. 530, Instituto de Ingeniería, Universidad Nacional Autónoma de México, Ciudad de México, Mexico (in Spanish).

Anderson, J. G., and S. E. Hough (1984). A model for the shape of the Fourier amplitude spectrum of acceleration at high frequencies, *Bull. Seismol. Soc. Am.* **74,** 1969–1993.

Arce, J. L., P. W. Layer, J. L. Macías, E. Morales-Casique, A. García-Palomo, F. J. Jiménez-Domínguez, J. Benowitz, and A. Vásquez-Serrano (2019). Geology and stratigraphy of the Mexico basin (Mexico City), central Trans-Mexican volcanic belt, *J. Maps* **15,** no. 2, 320–332, doi: 10.1080/17445647.2019.1593251.

Atkinson, G. M. (2015). Ground-motion prediction equation for small-to-moderate events at short hypocentral distances, with application to induced-seismicity hazards, *Bull. Seismol. Soc. Am.* **105,** 981–992.

Bayona-Viveros, J. A., G. Suárez, and M. Ordaz (2017). A probabilistic seismic hazard assessment of the Trans-Mexican volcanic belt, Mexico based on historical and instrumentally recorded seismicity, *Geofís. Int.* **56,** no. 1, 87–101.

Boore, D. M. (1983). Stochastic simulation of high-frequency ground motions based on seismological models of the radiated spectra, *Bull. Seismol. Soc. Am.* **73,** 1865–1894.

Boore, D. M. (2003). Simulation of ground motion using the stochastic method, *Pure Appl. Geophys.* **160,** 635–676.

Bouchon, M. (1981). A simple method to calculate Green's functions for elastic layered media, *Bull. Seismol. Soc. Am.* **71,** 959–971.

Brune, J. N. (1970). Tectonic stress and the spectra of seismic shear waves from earthquakes, *J. Geophys. Res.* **75,** 4997–5009.

Cruz-Atienza, V. M., A. Iglesias, J. F. Pacheco, N. M. Shapiro, and S. K. Singh (2010). Crustal structure below the Valley of Mexico estimated from receiver functions, *Bull. Seismol. Soc. Am.* **100,** 3304–3311, doi: 10.1785/0120100051.

Ego, F., and V. Ansan (2002). Why is the central Trans-Mexican volcanic belt (102°–99°W) in transtensive deformation? *Tectonophysics* **359,** 189–208.

Espíndola, V. H., L. Quintanar, and J. M. Espíndola (2017). Crustal structure beneath Mexico from receiver functions, *Bull. Seismol. Soc. Am.* **107,** 2427–2442, doi: 10.1785/0120160152.

Figueroa, J. (1971). *Sismicidad en la Cuenca del Valle de México*, Serie de Investigación, 289, Instituto de Ingeniería, UNAM, Mexico City, Mexico, 12 pp. (in Spanish).

Hartzell, S., L. Ramírez-Guzmán, M. Meremonte, and A. Leeds (2017). Ground motion in the presence of complex topography II: Earthquake sources and 3D simulations, *Bull. Seismol. Soc. Am.* **107,** 344–358, doi: 10.1785/0120160159.

Havskov, J. (1982). The earthquake swarm of February 1981 in Mexico City, *Geofís. Int.* **21,** no. 2, 157–175.

Havskov, J., and L. Ottemöller (1999). Electronic seismologist: SEISAN earthquake analysis software, *Seismol. Res. Lett.* **70,** 532–534.

Havskov, J., and S. K. Singh (1978). Shallow crustal structure below Mexico City, *Geofís. Int.* **17,** no. 2, 223–229.

Johnson, C. A., and C. G. A. Harrison (1990). Neotectonics in central Mexico, *Phys. Earth Planet. In.* **64,** 187–210.

Khors-Sansorny, C., F. Courboulex, M. Bour, and A. Deschamps (2005). A two-stage method for ground-motion simulation using stochastic summation of small earthquake, *Bull. Seismol. Soc. Am.* **95,** 1387–1400, doi: 10.1785/0120040211.

Lacan, P., M. Ortuño, L. Audin, H. Perea, S. Baize, G. Aguirre-Díaz, and R. Zúñiga (2018). Sedimentary evidence of historical and prehistorical earthquakes along the Venta de Bravo fault system, Acambay Graben (central Mexico), *Sediment. Geol.* **365,** 62–77, doi: 10.1016/j.sedgeo.2017.12.008.

Langridge, R., R. Weldon, J. Moya, and G. Suárez (2000). Paleoseismology of the 1912 Acambay earthquake and the

Acambay–Tixmadejé fault, Trans-Mexican volcanic belt, *J. Geophys. Res.* **105,** 3019–3037, doi: 10.1029/1999JB900239.

Langridge, R. M., M. Persaud, F. R. Zúñiga, G. J. Aguirre-Díaz, P. Villamor, and P. Lacan (2013). Preliminary paleoseismic results from the Pastores fault and its role in the seismic hazard of the Acambay graben, Trans-Mexican volcanic belt, *Mexico. Rev. Mex. Ciencias Geol.* **30,** 463–481.

Lermo, J., M. A. Santoyo, M. A. Jaimes, Y. Antayhua, and M. Chavacán (2016). Local earthquakes of the Mexico basin in Mexico City: κ, Q, source spectra, and stress drop, *Bull. Seismol. Soc. Am.* **106,** 1423–1437, doi: 10.1785/0120150189.

Manzanilla, L. (1986). Relación de los sismos ocurridos en la ciudad de México y sus efectos, *Rev. Mex. Sociol.* **4,** no. 2, 265–282 (in Spanish).

Maufroy, E., V. M. Cruz-Atienza, F. Cotton, and S. Gaffet (2015). Frequency-scaled curvature as a proxy for topographic site-effect amplification and ground-motion variability, *Bull. Seismol. Soc. Am.* **105,** 354–367, doi: 10.1785/0120140089.

Maufroy, E., V. M. Cruz-Atienza, and S. Gaffet (2012). A robust method for assessing 3-D topographic site effects: A case study at the LSBB underground laboratory, France, *Earthquake Spectra* **28,** 1097–1115, doi: 10.1193/1.4000050.

Maufroy, E., P. Lacroix, E. Chaljub, C. Sira, G. Grelle, L. Bonito, M. Causse, V. M. Cruz-Atienza, F. Hollender, F. Cotton, *et al.* (2018). Towards rapid prediction of topographic amplification at small scales: Contribution of the FSC Proxy and Pleiades Terrain Models for the 2016 Amatrice earthquake (Italy, M_w 6.0), *16th European Conf. on Earthquake Engineering*, Thessaloniki, Greece, 18–21 June 2018.

Mooser, F. (1972). The Mexican volcanic belt structure and tectonics, *Geofís. Int.* **12,** 55–70.

Ordaz, M., J. Arboleda, and S. K. Singh (1995). A scheme of random summation of an empirical Green's function to estimate ground motions from future large earthquakes, *Bull. Seismol. Soc. Am.* **85,** 1635–1647.

Ordaz, M., and S. K. Singh (1992). Source spectra and spectral attenuation of seismic waves from Mexican earthquakes, and evidence of amplification in the hill zone of Mexico City, *Bull. Seismol. Soc. Am.* **82,** 24–43.

Ortega, R., and L. Quintanar (2005). A study of the local magnitude scale in the Basin of Mexico: mutually consistent estimates of log A_0 and ground-motion scaling, *Bull. Seismol. Soc. Am.* **95,** 605–613, doi: 10.1785/0120030217.

Pasquaré, G., L. Vezzoli, and A. Zanchi (1987). Morphological and structural model of Mexican volcanic belt, *Geofís. Int.* **26**, no. 6, 159–176.

Quintanar, L., A. Cárdenas-Ramírez, D. I. Bello-Segura, V. H. Espíndola, J. A. Pérez-Santana, C. Cárdenas-Monroy, A. L. Carmona-Gallegos, and I. Rodríguez-Rasilla (2018). A seismic network for the Valley of Mexico: Present status and perspectives, *Seismol. Res. Lett.* **89,** no. 2A, 356–362, doi: 10.1785/0220170198.

Rosenblueth, E., M. Ordaz, F. J. Sánchez-Sesma, and S. K. Singh (1989). Design spectra for Mexico's federal district, *Earthq. Spectra* **5,** 258–272.

Singh, S. K., J. G. Anderson, and M. Rodríguez (1998). Triggered seismicity in the Valley of Mexico from major Mexican earthquakes, *Geofís. Int.* **37,** no. 1, 1–11.

Singh, S. K., R. Apsel, J. Fried, and J. N. Brune (1982). Spectral attenuation of *SH* waves along the Imperial fault, *Bull. Seismol. Soc. Am.* **72,** 2003–2016.

Singh, S. K., D. Arroyo, X. Pérez-Campos, A. Iglesias, V. H. Espíndola, and L. Ramírez (2017). Guadalajara, Mexico, earthquake sequence of December 2015 and May 2016: Source, Q, and ground motions, *Geofís. Int.* **56,** no. 2, 173–186.

Singh, S. K., A. Iglesias, D. García, J. F. Pacheco, and M. Ordaz (2007). Q of *Lg* waves in the central Mexican volcanic belt, *Bull. Seismol. Soc. Am.* **97,** 1259–1266.

Singh, S. K., A. Iglesias, M. Ordaz, X. Pérez-Campos, and L. Quintanar (2011). Estimation of ground motion in Mexico City from a repeat of the M ~ 7 : 0 Acambay earthquake of 1912, *Bull. Seismol. Soc. Am.* **101,** 2015–2028, doi: 10.1785/0120100317.

Singh, S. K., R. Quaas, M. Ordaz, F. Mooser, D. Almora, M. Torres, and R. Vásquez (1995). Is there truly a "hard" rock site in the Valley of Mexico? *Geophys. Res. Lett.* **22,** no. 4, 481–484.

Sokos, E., and J. Zahradnik (2008). ISOLA-A Fortran code and a Matlab GUI to perform multiple-point source inversion of seismic data, *Comput. Geosci.* **34,** 967–977.

Suárez, G., G. V. Caballero-Jiménez, and D. A. Novelo-Casanova (2019). Active crustal deformation in the Trans-Mexican volcanic belt as evidenced by historical earthquakes during the last 450 years, *Tectonics* **38,** no. 10, 3544–3562, doi: 10.1029/2019TC005601.

Suter, M., M. Carrillo-Martínez, M. López-Martínez, and E. Farrar (1995). The Aljibes half-graben active extension at the boundary between the Trans-Mexican volcanic belt and the Basin and Range Province, Mexico, *Geol. Soc. Am. Bull.* **107,** 627–641.

Suter, M., M. López-Martínez, O. Quintero-Legorreta, and M. Carrillo-Martínez (2001). Quaternary intra arc extension in the central Trans-Mexican volcanic belt, *Geol. Soc. Am. Bull.* **113,** 693–703, doi: 10.1130/0016-7606(2001)113<0693:QIAEIT>2.0.CO;2.

Suter, M., O. Quintero, and C. Johnson (1992). Active faults and state of stress in the central part of the Trans-Mexican volcanic belt. 1. The Venta de Bravo fault, *J. Geophys. Res.* **97,** no. 11, 983–11,994.

Suter, M., O. Quintero, M. López, G. Aguirre, and E. Ferrar (1995). The Acambay graben: Active intraarc extension in the Trans-Mexican volcanic belt, *Tectonics* **14,** 1245–1262.

Urbina, F., and H. Camacho (1913). La zona megasísmica de Acambay-Tixmadejé, Estado de México, conmovida el 19 de noviembre de 1912, *Bol. Inst. Geol. Méx.* **32,** 125 (in Spanish).

Waldhauser, F., and W. L. Ellsworth (2000). A double-difference earthquake location algorithm: method and application to the northern Hayward fault, California, *Bull. Seismol. Soc. Am.* **90,** 1353–1368.

Wells, D. L., and K. J. Coppersmith (1994). New empirical relationships among magnitude, rupture length, rupture width, rupture area, and surface displacement, *Bull. Seismol. Soc. Am.* **84,** 974–1002.

Manuscript received 23 March 2020
Published online 23 September 2020